Study of In-Line Capillary Fiber Sensor for Uniaxial Transverse Deformation

Arturo Sanchez-Gonzalez, Daniel Leandro, Romain Dauliat, Raphael Jamier, Philippe Roy, and Rosa Ana Perez-Herrera

***Abstract*—This research explores the impact of cyclic uniaxial transverse deformation on an in-line hollow-core fiber etalon. The structure consists of a 6 mm long section of capillary fiber spliced between two standard single-mode fibers. The optical response of the structure is theoretically analyzed in spectral and transformed domains, evidencing Fabry-Perot and antiresonant interferometric mechanisms. A validation of the theoretical behavior is carried out both through simulation and experimentation. The performance of the structure for uniaxial transverse deformation is subsequently evaluated by tracking the phase of the main component in the transformed domain. The relevance of measuring in the time domain is discussed, demonstrating improved accuracy over wavelength shift and inverse spatial domain methods. Several sensors with different internal diameters underwent cycles of transverse deformation, revealing robust linear trends in every case. On average, the structure demonstrated elastic behavior under deformations up to 42 μm, with a mean sensitivity of 0.174 rad/μm, and mechanical breakage taking place at 58 μm. The results confirmed the suitability of the sensor to withstand uniaxial micro-displacements or pressures, with smaller inner diameter capillary fibers showing the best performance.**

***Index Terms*—Antiresonant, capillary fiber, deformation, Fabry-Perot, fast Fourier transform, hollow core fiber, interferometer, optical fiber sensor, phase tracking, reflectance.**

I. Introduction

SINCE its initial conceptualization in the late 60s [1], a decade would prove sufficient for the fiber optic sensor technology to begin an expansion that would reach the present day [2]. The basic appeal behind this development involves the capability of modulating light signals within optical fibers in response to a variety of external parameters while preserving an inherent immunity to electromagnetic interference, lightweight, miniaturizable design, and ability to cover extensive distances without significant signal degradation [3]. Among the various types of fiber optic sensors, interferometric sensors, which rely on the superposition of light waves to measure minute changes in the optical path length induced by external stimuli, stand out for their unparalleled precision and sensitivity while preserving previous listed properties [4]. Such resilience paired with versatility has propelled their development for diverse critical application fields, namely civil engineering, medicine, defense, and seismology, amongst others [5], [6], [7], [8].

From a design point of view, most fiber optic interferometric sensors can be built both by employing standard single-mode fiber (SMF) combined with classical fiber components, as well as by hybrid structures in which segments of multimode, microstructured, or tapered fibers are placed between SMFs. The latter, commonly referred to as in-line fiber optic interferometric sensors, exploit the different guiding mechanisms in each fiber segment, as well as the existence of interfaces, to replicate classical interferometric mechanisms [9]. Of the aforementioned non-standard fibers, capillary fibers, characterized by an annular cross section of variable thickness and material, excel among the microstructured ones for their simplicity and low-cost [10]. As a result, capillary fibers, also known as hollow core fibers (HCFs) given their geometry, have recently been employed in the development of in-line fiber optic interferometric sensors for the monitoring of a wide range of physical and chemical parameters. Designs tailored for strain, temperature, curvature, refractive index, and liquid level have been recently reported [9], [11], [12], [13]. Despite the varied nature of measurands, their application in monitoring micro-deformation, pressure, and micro-displacement of the external medium remains largely unexplored. Furthermore, in most studies measurements are constrained to uniformly distributed pressures and deformations across the inner or outer surface of the fiber [14]. However, addressing a specific transverse direction becomes crucial in various applications, particularly when Hertzian contact is involved [15]. In these situations, the fiber may experience non-uniform stresses, or the installation might require adhesion to another surface, which is common in civil engineering projects involving structural health monitoring [16]. For reinforced concrete piled foundations of elevated and marine structures, which are typically subjected to significant inhomogeneous lateral forces,

Manuscript received 24 January 2024; revised 3 July 2024 and 1 August 2024; accepted 2 August 2024. Date of publication 6 August 2024; date of current version 16 September 2024. This work was supported in part by MCIN/AEI/10.13039/501100011033 and FEDER "A way to make Europe" under Project PID2019-107270RB-C22 and Project PID2022-137269OB-C21, in part by MCIN/AEI/10.13039/501100011033 and European Union "Next generation EU"/PRTR under Project PDC2021-121172-C21 and Project TED2021-130378B-C22, and in part by the Public University of Navarre under Project PJUPNA06-2022. Open access funding provided by Public University of Navarre. *(Corresponding author: Arturo Sanchez-Gonzalez.)*

Arturo Sanchez-Gonzalez, Daniel Leandro, and Rosa Ana Perez-Herrera are with the Department of Electrical, Electronic and Communications Engineering, and Institute of Smart Cities (ISC), Public University of Navarre, 31006 Navarre, Spain (e-mail: arturo.sanchez@unavarra.es; daniel.leandro@unavarra.es; rosa.perez@unavarra.es).

Romain Dauliat, Raphael Jamier, and Philippe Roy are with the XLIM UMR CNRS 7252, University of Limoges, F-87000 Limoges, France (e-mail: romain.dauliat@xlim.fr; raphael.jamier@xlim.fr; philippe.roy@xlim.fr).

Color versions of one or more figures in this article are available at https://doi.org/10.1109/JLT.2024.3438933.

Digital Object Identifier 10.1109/JLT.2024.3438933

traditional instrumentation includes inclinometers, pairs of conventional strain gauges, and displacement transducers at the pile head. However, recently, there has been a shift towards developing fiber-based schemes [17], where the capability to detect transverse pressures perpendicular to the pile surface is paired with the light weight, low cost, and electromagnetic immunity of the fiber. Moreover, reinforced concrete itself presents the limitation of being susceptible to corrosion. In this regard, recent designs have been proposed to address real-time corrosion spreading, relying on the monitoring of deformation fluctuations transversely and perpendicularly to the reinforcing steel and test fiber adherence surface [18].

From the point of view of the measurement technique, SMF-HCF-SMF structures rely on following one or several of the valleys or peaks of the interferogram to monitor the sensing parameter. However, since the effect of the external stimuli induces a wavelength shift of the spectrum in most cases, another natural option is to track the phase associated with the relevant contributions of the transformed spectrum obtained by means of the Fast Fourier Transform (FFT) algorithm. This alternative has several advantages, such as providing higher accuracy of the measurements and allowing the discrimination of the different interferometric components [19]. Nevertheless, this approximation requires prior identification of the underlying mechanisms in the interferogram to make the correct choice of components whose phase to track.

Taking all this into consideration, this work focuses on the analysis and design of a transverse deformation sensor based on capillary fibers that employs the phase tracking technique for an enhancement in accuracy. For this end, the research begins with the analysis of the multiple interferometric phenomena involved in a conventional SMF-HCF-SMF structure, subsequently focusing on those whose influence is predominant in the designed sensors. This study is performed both theoretically and through simulation, validating the conclusions reached with experimental results. Once the underlying interferometric phenomena have been thoroughly explained, the design and manufacturing process of the structure are optimized to minimize propagation losses while preserving a lengthy operating surface. After the experimental setup employed for the uniaxial transverse deformation study is presented, the measured interferogram and transformed spectra are studied to identify which parameter yields the best results. Sensors with different geometries are characterized under uniaxial transverse deformation cycles, achieving highly linear trends and sensitivities. Their performance is subsequently analyzed both globally and comparatively in terms of sensitivity, linearity, repeatability, and resilience. Finally, the relevance of employing the transformed temporal domain versus the inverse spatial domain in the enhancement of both estimator and measurement accuracy is discussed.

II. Theoretical Analysis and Simulation

Initially, a theoretical analysis supported by simulations have been performed in order to optimize and improve the design of the sensing structure. As a first approximation, a phenomenological approach to the different interferometric mechanisms supported by a SMF-HCF-SMF structure can be fulfilled by applying ray optics to any symmetry plane in which the optical axis of the system is contained [13]. For this purpose, once the light has travelled through the first SMF-HCF interface, each mode is replaced by a plane wave characterized by a wave vector k with an angle with respect to the optical axis ranging from 0 to that associated with the numerical aperture of the SMF. In this way, four different interferometric phenomena can be identified, as shown in the schematic illustration in Fig. 1 [10]. In the first place, the Fabry-Perot (FP) etalon associated with the existence of two interfaces facing each other (air-silica transition) is observed. As depicted by the solid green ray of Fig. 1, this phenomenon arises from the phase shift accumulation between consecutive roundtrips. Since the effective propagation along the optical axis can be conducted with a non-parallel k, simultaneous waves with different wave vectors will accumulate phase shifts depending on the difference in optical paths travelled, i.e., the difference in effective propagation constants. This indicates the existence of multimodal interference (MM), which can arise between waves traveling through the inner hollow core (solid rays in Fig. 1), between those traveling through the silica cladding of the capillary (dashed rays in Fig. 1), or between any combination of the two. In accordance with the literature [10], [13], the latter mechanism is referred to as Mach-Zehnder (MZ), given that each wave travels through a different physical medium. Finally, beyond a certain capillary length threshold [20], certain waves cross the cylindrical core-cladding interface of the HCF and, after returning to the hollow core, interfere with those remaining inside as illustrated by the dotted rays (yellow) in Fig. 1. This phenomenon results in a transverse confinement via destructive interference, in which wave attenuation coefficients go through periodic flat minima (antiresonances), reminiscent of the reflectance of a Fabry-Perot cavity with rotational symmetry [21]. Given that the actual propagation arises from an antiresonance (AR) mechanism instead of a proper guiding, this type of confinement, as well as the waveguide itself, receive the name of “leaky” [22].

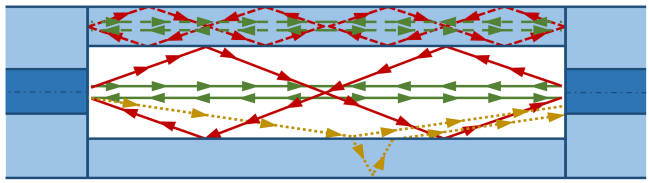

Fig. 1. Schematic illustration of the four interferometric phenomena supported by a SMF-HCF-SMF structure.

Once the distinct phenomena have been described, the particular influence of each mechanism on the overall performance of the structure highly depends on the dimensions of the HCF under consideration, requiring more precise models for their exploration. For this purpose, a complete electromagnetic model was considered through numerical computation. To begin with, the PhotoDesign suite of Fimmwave was employed for the simulation of the waveguide cross section in the semi-analytical

derivation of its modes. Once achieved, the determination of the SMF-HCF coupling matrix and mode propagation along the structure was carried out by means of Fimmprop, a numerical tool based on the EigenMode Expansion method. Considering the dimensions of the experimental manufacture, which will be detailed in the next section, the study analyzes structures with a capillary length (L) of 6 mm and an internal diameter (ID) ranging from 52.8 μm to 75 μm.

As the first remarkable result of simulation, the total power coupled from the SMF to the silica cladding of the HCF in the first interface remains well below 10^{-4}% in every case and over the entire S+C+L infrared band, making MZ and cladding MMI mechanisms negligible. Consequently, virtually all light is injected into modes confined mainly in the hollow core, which are therefore leaky as they present effective refractive indexes lower than the unit. Regarding the field distribution of these leaky modes, it closely resembles that of a guided mode found in a conventional waveguide [21]. For this reason, the mode numbering used henceforth refers exclusively to core modes, and it is specifically associated with the number of zeros of modal fields in the core, regardless of the field distribution in the claddings [22]. Considering that the structure is enclosed between two SMFs, with fundamental guided mode HE_{11}, only those leaky modes preserving symmetry could present coupling in the absence of axis mismatch or additional perturbations, i.e., HE_{1n} $\forall$ n $\in \mathbb{N}$. Simulation revealed that the first five modes HE_{11} to HE_{15} are enough to translate over 90% of the power injected into the HCF section of the structure in the spectral range from 182 to 207 THz (1450 to 1650 nm), with individual couplings varying between 5% and 35% depending on the particular mode, ID, and interrogation frequency. At the same time, being a leaky waveguide, propagation capabilities are highly limited by leakage loss, which greatly increases with modal index. To provide a sense of scale, the confinement loss incurred in propagation through a wavelength distance is over an order of magnitude greater for the second HE_{12} leaky mode than for the fundamental HE_{11} mode [23]. Therefore, and taking into account that the length of the leaky section of the sensor is 5 orders of magnitude greater than any operating frequency, it can be considered that the structure behaved as a single-mode waveguide (ignoring 2-fold polarization degeneracy). Note that the fundamental HE_{11} mode varied in nature from guided to leaky as SMF to HCF interfaces were crossed.

Consequently, of the four interferometric mechanisms initially proposed, only two retain significant impact: AR due to the leaky nature of the hollow waveguide, and FP as a consequence of performing the sensor characterization in reflection. In terms of its effect over reflectance, FP results in a spectral periodicity $\Delta\ \nu_{FP} = \ c/(2L)$ defined by the phase shift accumulation between successive roundtrips, $\phi_{FP} = \ 4\pi L\nu/c$ [24]. Similarly, AR leads to abrupt losses over the entire spectrum with periodicity $\Delta\ \nu_{AR} = \ c/(2d\sqrt{n_{cl}^2 - 1})$ related to the transverse geometry of the hollow waveguide and an accumulated phase shift $\phi_{AR} = \ 4\pi d\nu\sqrt{n_{cl}^2 - 1}/c$ [25]. In every case, c refers to the vacuum speed of light, ν is frequency, d is the thickness of the HCF silica cladding, and n_{cl} the refractive index of the HCF silica cladding. It is assumed that the latter matches the SMF cladding, therefore, being lower than SMF core refractive index n_{co}.

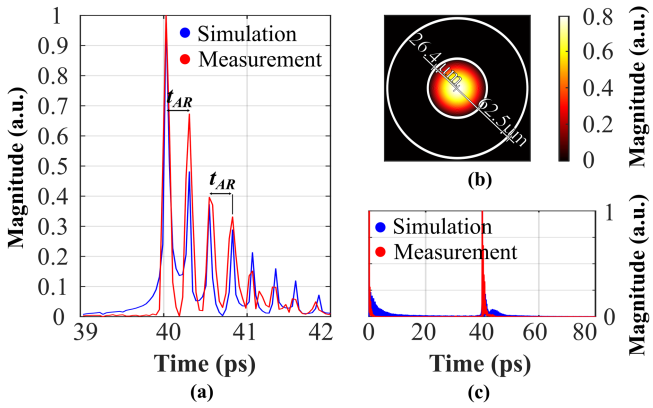

Fig. 2. Comparison of the experimental and simulation results obtained for the reflectance FFT magnitude in the range of the main contribution (a), with a wider span (c), and field distribution of the leaky HE_{11} mode obtained by semi-analytical computation (b).

Fig. 2(a) shows the main magnitude components in the transformed domain of the reflectance, obtained both experimentally and by simulation for an SMF-HCF-SMF structure of L = 6 mm and ID = 52.8 mum. As can be seen, contributions outside baseband of both experimental and simulated spectra perfectly matches. On the one hand, the main component in both cases corresponds with the FP behavior, $t_{FP} = \ \Delta\ \nu_{FP}^{-1} = \ 40$ ps. On the other hand, the AR contribution is present at evenly spaced intervals of $t_{AR} = \ \Delta\ \nu_{AR}^{-1} = \ 260$ fs. Only one contribution associated with FP is observable because, as a consequence of its low finesse, its effect can be fully described by a first-order Maclaurin series expansion without any loss of generality [24]. In contrast, this approximation is not applicable to the case of AR, where the transfer function is somewhat more intricate [10], promoting the presence of multiple spectral bands. This result is sometimes attributed to the multimodal nature of the structure [13]. However, this interferometric mechanism is not necessary for its derivation since the simulation shown here considers exclusively the fundamental HE_{11} mode, whose field distribution in the HCF is depicted in Fig. 2(b). Finally, contributions observable near DC in a wider temporal range as depicted in Fig. 2(c) reduce to the baseband replica of anti-resonance components, providing no additional information.

The comparison between experimental measurement and simulation was extended to structures with all four capillary diameters, presenting similar correspondence.

III. Experimental Setup

A. Sensor Design

Regarding the sensor configuration, a dimensioned diagram is illustrated in Fig. 3(a). The core element comprised a 6 mm long soft-glass high-silica capillary fiber segment spliced between two SMF sections. This length constraint, which defines the effective length of the sensor itself, was imposed to ensure that a mean reflectance exceeding 1% was experimentally achieved

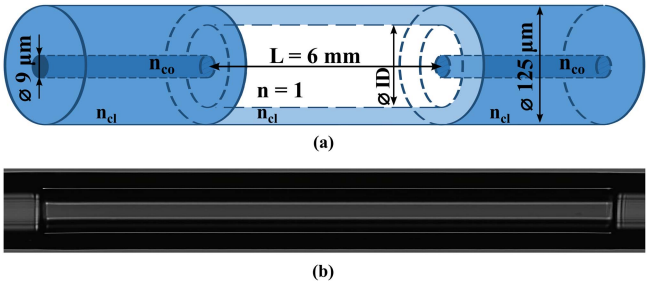

Fig. 3. Dimensional diagram of the designed sensor (a), and microscope image of one of the manufactured structures (b).

TABLE I
SENSOR MANUFACTURING PARAMETERS

PARAMETER	ID (µm)			
	52.8	55	66	75
Cleaving pre-strain (g)	209	205	192	180
Blade speed (µm/s)	50	50	46	42
Main arc power (bits)	STD – 85			
Main arc time (ms)	1800			
Rearc power (bits)	STD – 150			
Rearc time (ms)	1000			
Arc position over SMF (µm)	15	16	21	25
Fiber ends gap (µm)	5			

STD is the power required for SMF splicing under fusion splicer calibration.

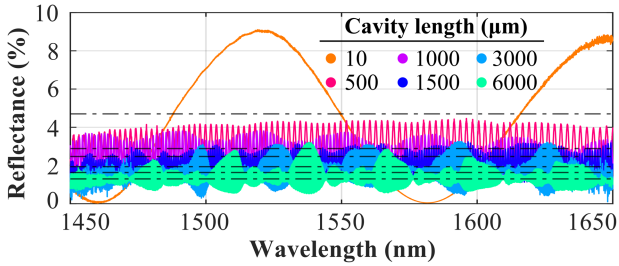

Fig. 4. Reflectance of SMF-HCF-SMF structures with ID = 52.8 μm and different cavity lengths.

across the spectral range from 1450 nm to 1650 nm, while maximizing the dimension over which transverse deformation would be applied. In reference to the silica capillary cross-section, the outer diameter (OD) was set at 125 μm, aligned with the cladding diameter of the SMF. Concerning the ID, different values were explored on the basis of three considerations. First of all, by significantly exceeding the mode field diameter of the employed SMF, insertion loss could be reduced in the SMF-HCF transition [10]. Secondly, given that the operating principle of the sensor relies mainly on the mechanical properties of capillary fibers, those associated with solid ring propagation and most affected by hollow core collapse during splices (MM and MZ) could be minimized by choosing a fairly large ID [26]. As a result, optical power would be mainly confined to the Fabry-Perot mechanism, albeit with the inherent influence of antiresonance as a consequence of the large capillary segment, well above the associated cut-off length [20]. Thirdly, the attenuation coefficient of any leaky mode in an HCF scales with ID^{-4} [22], requiring substantial IDs to achieve non-negligible mean reflectance over millimeter-in-length capillary section. As a trade-off between every constrain and manufacturing capabilities, sensors with HCFs characterized by IDs ranging from 50 to 75 μm were subjected to testing, namely 52.8, 55, 66 and 75 μm.

Soft-glass high-silica optical capillaries were designed and manufactured by means of conventional stack-and-draw technique, employing a pulling tower assembled for classical optical fibers and a single preform, where the different dimensional series were obtained following the premises set out in [27]. It is noteworthy that ID uniformity is not a limiting factor in the manufacturing process, as confinement losses remain within a factor of 2 under a 50% uncertainty in cladding thickness [23].

To ensure the creation of mechanically robust HCF-SMF interfaces without the occurrence of core collapse, axis misalignment, or fiber bending, a commercial specialty fiber fusion splicer (Fujikura FSM-100P) was employed. Among the different fusion parameters to be precisely set (discharge intensity profiles, number of cycles, and gap between the fiber ends), the influence of arc discharge location was particularly noteworthy to avoid core collapse. Thus, in order to consistently achieve homogenous and well-defined interfaces, the discharge had to take place from 15 to 25 microns over the SMF segment for internal diameters ranging from 50 to 75 μm. Similarly, to consistently achieve capillary fiber cleaves with angles below 0.5° and length uncertainties under the micrometer, a motorized microscopy-assisted electric cleaver station was employed (3SAE TMS). In this case, pre-strain the capillary before cleaving proved essential for straightness and uniformity, requiring a load range of 180 to 209 grams as ID decreased. The 1 μm movement resolution of the motorized clamps responsible for cleaving point alignment ensured that the uncertainty in the length of the HCF sensor section remained below the interrogation wavelength. Thus, considering the 6 mm length of the capillary sensor section imposed by reflectivity constraint, this resolution translated to a length error under 0.02%.

An optical microscope image of one of the manufactured devices can be partially observed in Fig. 3(b), while the specific fusion and cleaver parameters selected in the manufacturing process are detailed in Table I for the different IDs studied.

The reflectance of various fabrication examples with different capillary lengths for the specific case of ID = 52.8 μm are shown in Fig. 4, illustrating how both mean reflectance (represented by dashed lines), and minimum visibility or extinction ratio (ER), degrade as capillary length is increased. Thus, in the transition from 10 to 6000 μm there is a decrease from 4.7% to 1.3% in mean reflectance and a deterioration in the minimum ER from 9% to 0.15%. These results highlight the critical trade-off between maximizing sensor length to enhance the deformable effective area and hence sensitivity, while achieving a visible interferogram rather than a flat and negligible reflectance curve. Therefore, the sensor length was limited to 6 mm to ensure a mean reflectance exceeding 1% within the 1450 nm to 1650 nm interrogation range.

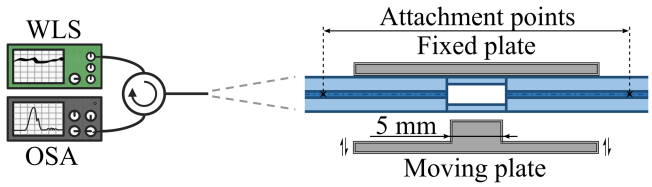

Fig. 5. Experimental setup employed during SMF-HCF-SMF sensor characterization.

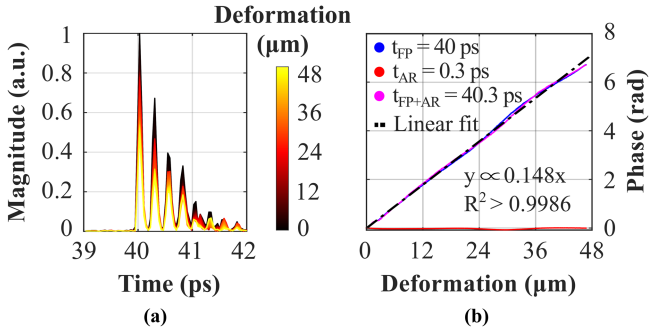

Fig. 6. Evolution of the FFT spectra magnitude (a), and main phase components (b), with uniaxial transverse deformation. Case of the sensor with ID = 52.8 μm.

B. Interrogation Scheme

In order to test the interferometric structure as transverse deformation sensor, the interrogation scheme depicted in Fig. 5 was employed in the experiments. As illustrated, a broadband white light source (WLS) providing an integrated output power of 7.55 mW from 1450 to 1650 nm and an optical spectrum analyzer (OSA, Anritsu MS9740A) with a spectral resolution of 0.03 nm were employed. Given that sensor monitoring was performed in reflection, a conventional C-band circulator was introduced to redirect the light coming from the source once reflected from the sensor back to the OSA. However, considering the wide range of interrogation and the narrow bandpass and insertion losses of the circulator, measurements were referenced to the response of a calibration mirror with a flat reflectance in the S+C+L band. Furthermore, to prevent undesired reflections, the free end of the SMF section of the sensor remained immersed in an index-matching gel.

In reference to the actuator used to apply uniaxial transverse deformation, a pair of grips, positioned at a fixed distance of 25 cm from each other, were employed to secure and center the sensor onto a flat polished sheet. The sensing fiber was pre-strained before fixing with a 0.15 N load. Facing it, another 5 mm-long flat surface approach and withdraw from the sensor in predefined patterns, applying cyclic uniaxial transverse deformation to the sensors. The motorized unit employed for surface spacing control exhibited a resolution of 204 $\pm$ 17 nm, which established the step resolution for the progressively increased consecutive deformation and relaxation cycles.

Given the length of moving plate and sensor, the deformation was purposefully confined to the capillary section of the structure, avoiding any disturbance of the SMF cross section that could interfere with the measurement process. Additionally, this limitation in stress applied to the splices served to minimize the risk of structural failure, thereby mitigating potential shortening of the measuring range.

IV. Results and Discussion

A. Uniaxial Transverse Deformation Characterization

At each step within each deformation-relaxation cycle, reflectance data from the sensor was captured within the spectral range of 182 to 207 THz (1450 to 1650 nm). Following, FFT was directly applied over the frequency axis spectrum. Upon obtaining reflectance in the Fourier-transformed domain, its evolution with incremental values of uniaxial transverse micro-deformation was studied.

Concerning the magnitude of the FFT spectra, it can be observed in Fig. 6(a) (ID = 52.8 μm), that FP and AR components maintained a constant profile, suffering exclusively from attenuation as the fiber geometry was altered. Therefore, their phase could be reliably monitored as a source of information, resulting in Fig. 6(b). As depicted, both FP and FP+AR main components exhibited remarkable phase linearity with transverse deformation, with a determination coefficient $R^2 > 0.9986$. Consequently, the sensitivities measured are for FP and FP+AR $1.48 \cdot 10^{-1} \pm 1.0 \cdot 10^{-3}$ rad/μm and $1.48 \cdot 10^{-1} \pm 1.2 \cdot 10^{-3}$ rad/μm, which can be considered statistically indistinguishable. This result extended to the remaining replicas of AR over FP, since they all inherited the sensitivity of FP because of the negligible sensitivity of AR with applied stress, remaining two orders of magnitude below the FP case. This experimental independence of AR with uniaxial transverse deformation is in agreement with theoretical results, whereby the spectral response depends exclusively on the thickness of the circular ring [21], unaltered during measurements. Additionally, this insensitivity of the AR temporal component phase to transverse micro-deformation allows for immediate multiparametric discrimination of other physical magnitudes that produce wavelength shifts in AR, such as temperature [28]. For this purpose, any two of the three temporal components represented in Fig. 6(b) can be employed to extract the sensitivity matrix following the process described in [29].

The study was repeated for structures with all four capillary diameters, yielding consistent results in every case between the interferometric contributions and their phase evolution.

B. Phase Tracking During Deformation Cycles

Based on the previous findings, the main FFT component of each sensor was chosen for tracking its phase response under applied deformation. The outcome is presented in Fig. 7, where the consecutive and progressively increased deformation-relaxation cycles are depicted in black. The reference line at 0 μm marks the contact between the motorized flat surface and the outer surface of each sensor. Consequently, positive values correspond to progressive transverse deformation, leading to a reduction in the capillary fiber diameter along that specific transverse axis while increasing its eccentricity. For each sensor

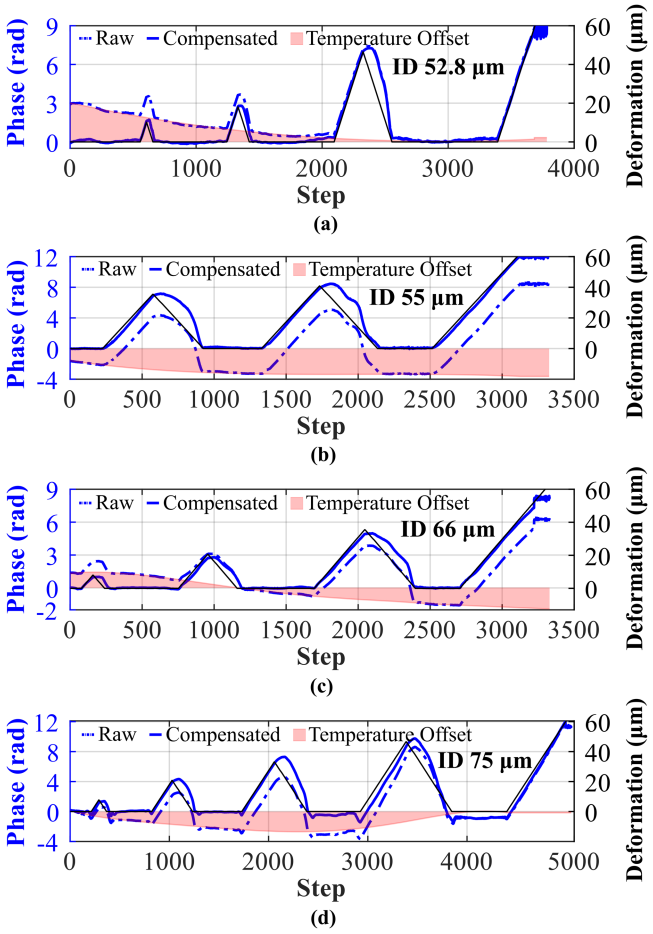

Fig. 7. Phase variation of the time-FFT main contribution as a result of progressive uniaxial transverse deformation cycles for the sensor with an HCF characterized by an ID of 52.8 μm (a), 55 μm (b), 66 μm (c), and 75 μm (d).

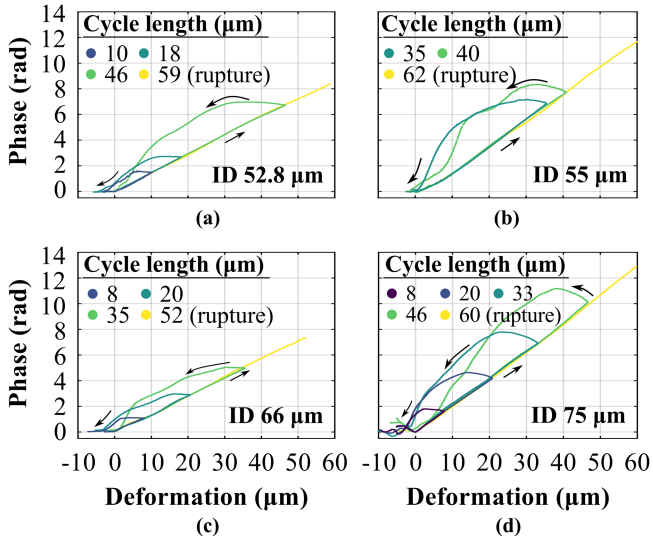

Fig. 8. Phase hysteresis cycles after temperature compensation as a result of increasingly uniaxial transverse deformation cycles for the sensor with an HCF characterized by an ID of 52.8 μm (a), 55 μm (b), 66 μm (c), and 75 μm (d).

TABLE II
SENSOR CHARACTERIZATION RESULTS

ID (µm)	$\bar{S}$ (rad/µm)	CV (%)	R^2_{min}
52.8	0.147	1.2	0.9952
55	0.202	0.5	0.9950
66	0.137	3.1	0.9937
75	0.209	6.0	0.9988

ID is the capillary internal diameter. $\bar{S}$ is the sensitivity averaged over the different deformation cycles. CV is the coefficient of variation of the mean sensitivity. R^2_{min} is the minimum coefficient of determination obtained between every linear regression of each sensor.

and cycle, the background of the blue dashed curve reveals that the phase was notoriously influenced by variations in room temperature, consistent with observations in similar hollow-core fiber (HCF) structures of a certain length [11]. However, by inducing deformation at a high rate compared to the slowly varying nature of ambient temperature, the characteristic times of both phenomena differ enough to consider the temperature quasi-static during the deformation process. This was the case in the experiments conducted, where temperature fluctuations caused a phase variation of 3.2 mrad/step at most, compared to 26 mrad/step induced by deformation as the bare minimum. Consequently, the influence of temperature remained more than eight times lower than that of deformation, allowing it to be considered constant during the deformation-relaxation ramps. Nonetheless, to further acknowledge for its influence, large time intervals without applying deformation were monitored between each experimental deformation-relaxation curve. This data was employed to perform a polynomial fit of the phase within these non-deformation measurement segments, which was finally subtracted from the total phase data as an offset compensation. The results are depicted in solid blue, showing that the phase of the main central frequency component of every sensor faithfully tracked the upward deformation ramps, displaying marginally longer relaxation times during the downward ramps. In each cycle, the phase ultimately returned to its initial resting value until the last ramp, where sensors were subjected to a stress test until breakage. These observations are similarly depicted in Fig. 8, illustrating the various hysteresis cycles undergone by the sensor.

As it is summarized in Table II by means of the different coefficients of determination, each monitored phase component exhibited a strong linear trend with progressively applied deformation. These findings surpassed those recently reported by authors on similar structures [30], showcasing a fourfold increase in mean uniaxial transverse deformation sensitivity, $\bar{S}$. Furthermore, the sensitivity remained consistently stable across cycles, independently of the HCF employed, with a maximum coefficient of variation (CV) of 6% for the 75 μm scenario. This sensitivity also exhibited strong linearity in all cases, with a coefficient of determination of $R^2 > 0.994$. This result exceeds those of recent studies based on the characterization of unidirectional microstrain and microdisplacement employing other fiber optic technologies, such as designs based on specialty fibers like fused polymer fibers [31] and photopolymer fibers [32], with R^2 ranging from 0.912 to 0.985, or more classical designs based

on suspended-core [33] and FBG-based sensors [34], [35], with $R^2 < 0.972$.

Several significant conclusions can be drawn by comparing the different results obtained for each sensor in Table II. Firstly, the sensitivity of the structure did not show a direct dependence on the internal capillary diameter, resulting in similar outcomes across the entire range of internal diameters. Secondly, the repeatability of measurements with consecutive deformation cycles seemed to worsen with the capillary diameter, as indicated by the coefficient of variation (CV). This could be related to the emergence of micro-fractures in the HCF structure as induced stress accumulated, with sensors becoming more susceptible as the solid circular crown diminished. The example that best illustrates this behavior is precisely the sensor with an ID of 75 μm, whose sensitivity increased by 3% between successive cycles from the second onwards. It is finally noteworthy that, although every HCF underwent a deformation over 50 μm before rupture, the cases with 52.8 and 55 μm withstood deformations up to a 112% of their ID, involving the complete hollow core collapse. This deformation range falls within those reported in recent studies concerning transverse microdisplacements and deformations, spanning from 6 μm [32], 380 μm [33], to a limit of 1.1 mm by auxiliary employing textile elastic pads to shield the test fiber [34]. However, in all these cases, the measurement resolutions ranged between 0.45 and 1 μm, which implies a decline by a factor of 2 to 4 with respect to the SMF-HCF-SMF results presented in this study. All these findings underscore the highly elastic nature of the structure and its suitability as a robust transverse micro-deformation sensor, but mostly for those cases with a smaller ID.

C. Inverse Spatial- vs. Time- Transformed Domain

In recent studies, in the pursuit of a precision enhancement in identifying the spectral components of classical interferometric structures [19], [33], and capillary-based fiber interferometers [10], [11], [12], [30], the Fourier transform has been commonly applied to the wavelength spectrum, thus working in the inverse spatial domain (also referred as spatial-frequency domain). However, it is clear from the analytical expressions of ϕ_{FP} and ϕ_{AR} that the free spectral range (FSR) of both interferometric phenomena lacks linearity with wavelength. Under some conditions, such as reduced spectral windows, this behavior can also be assumed linear in wavelength, yielding accurate results. In contrast, this assumption has some detrimental implications in cases where the FSR varies enough along the analyzed spectrum. Then, the FFT does not provide a clear peak (or peaks if several spectral contributions are present). Actually, there is a spectral spreading that might mix the FFT contributions, which, influenced by the phase terms, can prevent the correct and accurate identification of several interferometric phenomena. This effect is common in SMF-HCF-SMF structures.

For instance, in this work, the FSR_{FP} for the sensors designed varies from 175 pm at $\lambda = 1450$ nm to 230 pm at $\lambda = 1650$ nm, representing an increase of up to 30% from its initial value. As mentioned, this is the result of FSR_{FP} being a continuously variable function, quadratic in wavelength. Consequently, if we directly apply the FFT to the wavelength domain, the significant inverse spatial frequencies in the transformed domain will be distributed in a wide interval $\xi^{FP} \in [4.405,\ 5.7143]\,\text{nm}^{-1}$, resulting in the overlapping of the different interference phenomena (FP, AR, and MMI if present) within the same window of spatial frequencies, making the domain unsuitable for studying this type of interferometric structures. This spectral spreading and overlapping effect can be seen in the blue line of Fig. 9 for one of the studied sensors. However, based on the previous analytical expressions and remaining interferometric phenomena observable in SMF-HCF-SMF structures [10], [13], it can be noticed that, regardless of the spectral window or geometry of the structure, the FSRs of all interferometric phenomena are constant and unique in the frequency domain, as presented in Section II. Therefore, in the time-FFT domain, it arises a clear criterion for selecting unique contributions whose phase to monitor, as each interferometric phenomenon is perfectly identified and detached from the others (Fig. 9 red line). Besides the contribution identification, this is particularly important for sensing applications where the phases of FFT peaks are monitored.

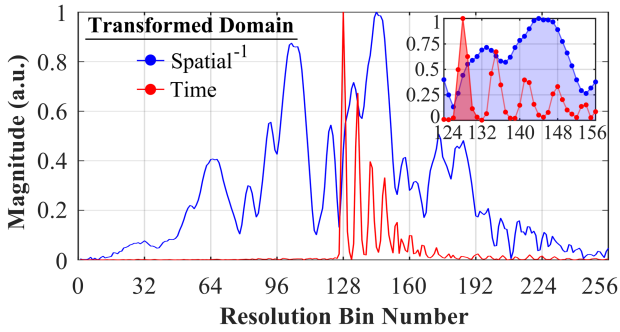

Fig. 9. Comparison of the resolution achieved under spatial- and time- FFT data processing for the reflectance of the sensor with ID = 52.8 μm.

To demonstrate the improved accuracy and reliability in using the time-transformed domain to select the estimator to monitor, it is particularly illustrative to simultaneously plot the magnitudes resulting from applying the Fourier transform directly over same experimental data, both in wavelength and frequency spectrum. To achieve this, we unify the abscissa axis as resolution bins. The result is shown in Fig. 9, where it can be observed, primarily through the inset, that the contribution associated with FP changes from being indeterminate to being fully integrated into a single peak.

Moreover, this domain duality significantly affects measurement accuracy, while preserving sensitivity. To evaluate it, the phase response to progressive deformation for the same experimental data is compared using three methods:

- Tracking the wavelength shift of three main fringes on the reflectance spectrum, and subsequently converting them to phase by dividing by the FP period at that wavelength (so that the resulting physical quantity is phase, comparable to the following two cases).
- Tracking the phase of three main components in the spatial-FFT domain.

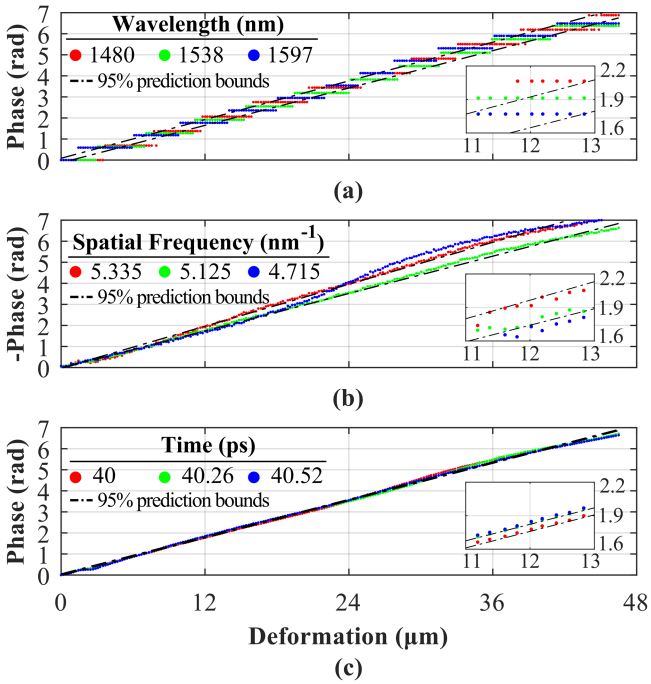

Fig. 10. Comparison of the results obtained from the same monitoring data of the sensor with ID = 52.8 μm under direct wavelength shift measurement (a), spatial-FFT phase tracking (b), and time-FFT phase tracking (c).

- Tracking the unique component t_{FP} and, for completeness, the first two harmonics of the AR modulation, $t_{FP} + t_{AR}$ and $t_{FP} + 2t_{AR}$, in the time-FFT domain.

The results of this process are shown in Fig. 10. As illustrated, in the case of directly tracking the wavelength shift as in Fig. 10(a), there is a clear limitation by the spectral resolution in comparison with Fig. 10(b) and (c) techniques, showing a maximum coefficient of determination $R^2 = 0.9886$ and, notably, significant dispersion depending on the specific peak studied, with sensitivities ranging from 0.149 rad/μm to 0.155 rad/μm. Similarly, although showing better resolution, tracking a peak in the transformed spatial-frequency domain also proves highly sensitive to the specific monitored peak (Fig. 10(b)). In this regard, the coefficients of determination range from $R^2 = 0.9871$ to $R^2 = 0.9958$, and sensitivities vary from 0.142 rad/μm to 0.171 rad/μm, evidencing the impact of an appropriate peak selection also in the achieved sensitivity. However, there is no visual clue on the FFT spectrum of which components should be monitored due to the spectral spreading. Finally, the transformed temporal spectrum achieves higher coefficients of determination, exceeding $R^2 = 0.9986$ in all cases, with a statistically indistinguishable sensitivity of 0.148 rad/μm for all estimators (Fig. 10(c)). It is also important to note that, while three reflectance fringes and three spatial-FFT peaks were chosen, they do not differ in interferometric nature from the others. Thus, no theoretical preference criterion can be established. Instead, in the case of the temporal transform, we could have limited the measurement to the contribution t_{FP}. As stated, this is the result of interferometric phenomena contributions being perfectly detached, and therefore identifiable, in the time-FFT domain.

These results demonstrate the improvement in both estimator and measurement accuracy by measuring in the temporal transformed domain over the spatial domain. This should be considered in particular for interferometric structures with non-negligible FSR changes along the measured spectrum and with multiple contributions.

V. Conclusion

This work has studied the impact of cyclic uniaxial transverse deformation on an in-line hollow-core fiber etalon. The structure comprises a 6 mm long hollow-core fiber spliced to standard single-mode fiber at both ends. Multiple capillary fibers with different inner diameters where considered, optimizing the manufacturing process to achieve a mean reflectance exceeding 1% within the 1450 nm to 1650 nm interrogation range for every case. The expected optical response in the spectral and transformed domains were theoretically analyzed, emphasizing in the Fabry-Perot and antirresonant interferometric mechanisms experienced by the waveguide, as well as its mainly single-mode nature. This analysis was verified both experimentally and by simulation, characterizing its behavior in time-dependent Fourier-transformed domain by means of the FFT algorithm. Subsequently, the phase of the central main FFT component of the reflectance was continuously monitored through successive uniaxial transverse deformation and relaxation cycles of progressively increasing magnitude, up to the point of sensor breakage. The outcomes revealed robust linear trends with consistent sensitivities in each deformation cycle, reliably returning to the same initial resting value during the relaxation phase of each cycle. Ultimately and on average, the developed structure demonstrated elastic resilience to deformations of up to 42 μm, exhibiting a mean sensitivity of 0.174 rad/μm, before reaching rupture at 58 μm. Thus, the capability of the structure to robustly endure uniaxial micro-displacements or pressures was proved. Although every capillary fiber among those considered resulted in a reliable sensor, the performance of those with a smaller inner diameter excelled. Finally, the relevance of measuring in the time-FFT domain was discussed, demonstrating both estimator and measurement accuracy enhancement compared with classical wavelength shift and spatial-FFT approaches.

References

[1] C. Menadier, C. Kissenger, and H. Adkins, "The fotonic sensor," *Instrum. Control Syst.*, vol. 40, 1967, Art. no. 114.

[2] V. Vali and R. W. Shorthill, "Fibre ring interferometer," *Appl. Opt.*, vol. 15, no. 5, pp. 1099–1100, May 1976, doi: 10.1364/AO.15.001099.

[3] B. Culshaw, "Optical fiber sensor technologies: Opportunities and-perhaps-pitfalls," *J. Lightw. Technol.*, vol. 22, no. 1, pp. 39–50, Jan. 2004, doi: 10.1109/JLT.2003.822139.

[4] B. H. Lee et al., "Interferometric fiber optic sensors," *Sensors*, vol. 12, no. 3, pp. 2467–2486, Feb. 2012, doi: 10.3390/s120302467.

[5] T. Y. Cosgun et al., "Miniaturised gap sensor using fibre optic Fabry-Pérot interferometry for structural health monitoring," *Opt. Exp.*, vol. 30, no. 24, pp. 42923–42932, Nov. 2022, doi: 10.1364/OE.462070.

[6] T. E. Tabaru, A. Karatutlu, and B. Ortaç, "Phase-shifted Bragg-grating consisting of silicon oxynitride doped silicon and silica alternating layers lab-on-fiber for biosensors with ultrahigh sensitivity and ultralow detection limit," *Opt. Laser Technol.*, vol. 167, Dec. 2023, Art. no. 109693, doi: 10.1016/j.optlastec.2023.109693.

[7] S. E. Hayber, T. E. Tabaru, S. Keser, and O. G. Saracoglu, "A simple, high sensitive fiber optic microphone based on cellulose triacetate diaphragm," *J. Lightw. Technol.*, vol. 36, no. 23, pp. 5650–5655, Dec. 2018, doi: 10.1109/JLT.2018.2878345.

[8] T. Chang et al., "Fiber optic interferometric seismometer with phase feedback control," *Opt. Exp.*, vol. 28, no. 5, pp. 6102–6122, Feb. 2020, doi: 10.1364/OE.385703.

[9] T. Zhu, D. Wu, M. Liu, and D.-W. Duan, "In-line fiber optic interferometric sensors in single-mode fibers," *Sensors*, vol. 12, no. 8, pp. 10430–10449, Aug. 2012, doi: 10.3390/s120810430.

[10] W. Sun et al., "Comparative study on transmission mechanisms in a SMF-capillary-SMF structure," *J. Lightw. Technol.*, vol. 38, no. 15, pp. 4075–4085, Aug. 2020, doi: 10.1109/JLT.2020.2983910.

[11] R. A. Perez-Herrera, M. Bravo, D. Leandro, S. Novais, J. Pradas, and M. Lopez-Amo, "Multiparameter sensor based on a multi-interferometric serial configuration for temperature and strain measurements," *IEEE J. Sel. Topics Quantum Electron.*, vol. 27, no. 6, Nov./Dec. 2021, Art. no. 5600704, doi: 10.1109/JSTQE.2021.3072163.

[12] L. A. Herrera-Piad, I. Hernández-Romano, D. A. May-Arrioja, V. P. Minkovich, and M. Torres-Cisneros, "Sensitivity enhancement of curvature fiber sensor based on polymer-coated capillary hollow-core fiber," *Sensors*, vol. 20, no. 13, Jul. 2020, Art. no. 3763, doi: 10.3390/s20133763.

[13] Z. Huang et al., "Light transmission mechanisms in a SMF-capillary fiber-SMF structure and its application to bi-directional liquid level measurement," *Opt. Exp.*, vol. 30, no. 12, pp. 21876–21893, Jun. 2022, doi: 10.1364/OE.456917.

[14] G. Salceda-Delgado, A. Van Newkirk, J. E. Antonio-Lopez, A. Martinez-Rios, A. Schülzgen, and R. Amezcua-Correa, "Optical capillary fiber mode interferometer for pressure sensing," *IEEE Sens. J.*, vol. 20, no. 5, pp. 2253–2260, Mar. 2020, doi: 10.1109/JSEN.2019.2953683.

[15] K. L. Johnson, "Normal contact of elastic solids – Hertz theory," in *Contact Mechanics*, 1st ed. Cambridge, U.K.: Cambridge Univ. Press, 1985, ch. 4, pp. 84–106.

[16] A. Loayssa, "Optical fiber sensors for structural health monitoring," in *New Developments in Sensing Technology for Structural Health Monitoring*, 1st ed. Berlin, Germany: Springer, 2011, ch. 14, pp. 335–358.

[17] Y. P. Oh, P. H. Ooi, Y. L. Ñee, H. H. W. Oscar, and K. W. Wong, "Lateral load test on bored cast in-situ pile instrumented with distributed fiber optic strain sensors," in *Smart Geotechnics for Smart Societies*, 1st ed. Boca Raton, FL, USA: CRC Press, 2023, pp. 1403–1408.

[18] C. McCague et al., "Novel sensor design using photonic crystal fibres for monitoring the onset of corrosion in reinforced concrete structures," *J. Lightw. Technol.*, vol. 32, no. 5, pp. 891–896, Mar. 2014, doi: 10.1109/JLT.2013.2293120.

[19] D. Leandro, M. Bravo, and M. Lopez-Amo, "High resolution polarization-independent high-birefringence fiber loop mirror sensor," *Opt. Exp.*, vol. 23, no. 24, pp. 30985–30990, Nov. 2015, doi: 10.1364/OE.23.030985.

[20] X. Zhang et al., "Transition of Fabry–Perot and antiresonant mechanisms via a SMF-capillary-SMF structure," *Opt. Lett.*, vol. 43, no. 10, pp. 2268–2271, May 2018, doi: 10.1364/OL.43.002268.

[21] J.-L. Archambault, R. J. Black, S. Lacroix, and J. Bures, "Loss calculations for antiresonant waveguides," *J. Lightw. Technol.*, vol. 11, no. 3, pp. 416–423, Mar. 1993, doi: 10.1109/50.219574.

[22] M. Miyagi and S. Nishida, "Transmission characteristics of dielectric tube leaky waveguide," *IEEE Trans. Microw. Theory Techn.*, vol. TMTT-28, no. 6, pp. 536–541, Jun. 1980, doi: 10.1109/TMTT.1980.1130115.

[23] D. Bird, "Attenuation of model hollow-core, anti-resonant fibres," *Opt. Exp.*, vol. 25, no. 19, pp. 23215–23237, Sep. 2017, doi: 10.1364/OE.25.023215.

[24] J. L. Santos, A. P. Leite, and D. A. Jackson, "Optical fiber sensing with a low-finesse Fabry–Perot cavity," *Appl. Opt.*, vol. 31, no. 34, pp. 7361–7366, Dec. 1992, doi: 10.1364/AO.31.007361.

[25] C.-H. Lai et al., "Modal characteristics of antiresonant reflecting pipe waveguides for terahertz waveguiding," *Opt. Exp.*, vol. 18, no. 1, pp. 309–322, 2010, doi: 10.1364/OE.18.000309.

[26] R. Marchetti, C. Lacava, L. Carroll, K. Gradkowski, and P. Minzioni, "Coupling strategies for silicon photonics integrated chips [invited]," *Photon. Res.*, vol. 7, no. 2, pp. 201–239, Feb. 2019, doi: 10.1364/PRJ.7.000201.

[27] R. Romaniuk, "Capillary optical fiber - design, fabrication, characterization and application," *Bull. Polish Acad. Sci., Tech. Sci.*, vol. 56, no. 2, pp. 87–102, Jun. 2008.

[28] T. Nan et al., "Three-parameter measurement optical fiber sensor based on a hybrid structure," *Appl. Opt.*, vol. 59, no. 27, pp. 8190–8195, Sep. 2020, doi: 10.1364/AO.401652.

[29] A. Sanchez-Gonzalez et al., "A dual-wavelength fiber laser sensor with temperature and strain discrimination," *Sensors*, vol. 22, no. 18, Sep. 2022, Art. no. 6888, doi: 10.3390/s22186888.

[30] A. Sanchez-Gonzalez et al., "Micro-displacement sensor based on hollow core fiber interferometers," presented at 27th International Conference on Optical Fiber Sensors, Alexandria, VA, USA, Aug. 29–Sep. 02, 2022, Paper Th4.10.

[31] A. Leal-Junior et al., "Strain, temperature, moisture, and transverse force sensing using fused polymer optical fibers," *Opt. Exp.*, vol. 26, no. 10, pp. 12939–12947, May 2018, doi: 10.1364/OE.26.012939.

[32] F. Zhang et al., "A novel micro-displacement sensor based on double optical fiber probes made through photopolymer materials," *Materials*, vol. 12, no. 23, Dec. 2020, Art. no. 5475, doi: 10.3390/ma13235475.

[33] M. Bravo, A. M. R. Pinto, M. Lopez-Amo, J. Kobelke, and K. Schuster, "High precision micro-displacement fiber sensor through a suspended-core Sagnac interferometer," *Opt. Lett.*, vol. 37, no. 2, pp. 202–204, Jan. 2012, doi: L10.1364/OL.37.000202.

[34] F. Urban, J. Kadlec, R. Vlach, and R. Kuchta, "Design of a pressure sensor based on optical fiber Bragg grating lateral deformation," *Sensors*, vol. 10, no. 12, pp. 11212–11225, Dec. 2010, doi: 10.3390/s101211212.

[35] Q. Jiang and D. Hu, "Microdisplacement sensor based on tilted fiber Bragg grating transversal load effect," *IEEE Sensors J.*, vol. 11, no. 9, pp. 1776–1779, Sep. 2011, doi: 10.1109/JSEN.2010.2103399.